

# Supplementary Materials for Dual-diffusion with Physical Correction for EIT Image Reconstruction

Zichen Wang, Tao Zhang, Luxiang Xie, Xinyu Zhang, Chi-Sheng Chen, Xiaoyan Chen, Qi Wang

**Abstract**—This document is the additional part of the main manuscript ‘Dual-diffusion with Physical Correction for EIT Image Reconstruction’, which is the *Supplementary Materials*. In this material, we firstly give the related backgrounds and preliminaries including the sensing principle of electrical impedance tomography (EIT), the score-based diffusion model with SDE framework as the EIT inverse problem solver, and the basic knowledge of Schrödinger Bridge (SB) and image-to-image SB ( $I^2$ SB). Secondly, we provide more details of training datasets, such as the geometry and conductivities configuration of simulated information. Next, more reconstruction results are provided in this document. For example, the static experiments with tank phantom and the out-of-distribution with public benchmark and dynamic experiment are given, which comprehensively demonstrate the performance between our dual diffusion-based framework combined with a physical correction ( $D^2$ PC-EIT) and other comparisons based on unsupervised generation strategy. Finally, the related works are fully reviewed from the following aspects, such as the learning-based EIT reconstruction methods, the diffusion-based methods for solving inverse imaging problems, and the SB-based solvers in low-level vision tasks. The main distinctions between  $D^2$ PC-EIT and competing methods are listed.

The multimedias for visualizing the dynamic reconstructions are given in [Github Project: D<sup>2</sup>PC-EIT](#).

**Index Terms**—EIT, inverse problem, diffusion models, Schrödinger Bridge, physical correction.

## I. BACKGROUNDS AND PRELIMINARIES

In this section, we mainly review the backgrounds and knowledge from the following aspects: the sensing principle of EIT, the mathematical formulation of Schrödinger Bridge (SB) and image-to-image SB ( $I^2$ SB).

### A. EIT sensing principle and forward problem

In this paper, we consider a two-dimension EIT observation model, as shown in Figure 1. Let  $\Omega$  be an observation domain in  $\mathbb{R}^2$  with a boundary  $\partial\Omega$ . The set of electrodes  $\{e_l\}_{l=1}^L$  which are attached on the boundary  $\partial\Omega$  with an equal distance. The alternating current  $I_l$  with certain frequency is injected from the  $L$ -th electrode into the observation domain  $\Omega$  (with conductivity distribution  $\sigma(x)$  and  $x$  denotes the position) to generate induced potential  $u(x)$  and measure the signal responding on the other electrodes. For an EIT sensing system containing  $L$  electrodes, a total of  $L \times (L - 3)$  effective voltages are measured for reconstructing one frame of the conductivity distribution.

**Zichen Wang, Tao Zhang, and Qi Wang (corresponding author)** are with the School of Electronic and Information Engineering, Tiangong University, Tianjin 300387, China. **Luxiang Xie** is with the School of Clinical Medicine, Tsinghua University and Department of Engineering Physics, Tsinghua University, **Xinyu Zhang** is with The Luddy School, Indiana University Bloomington, Bloomington, IN 40478, USA. **Chi-Sheng Chen** is with the Beth Israel Deaconess Medical Center, Harvard University, USA. **Xiaoyan Chen** is with the College of Electronic Information and Automatic, Tianjin University of Science and Technology, Tianjin, 300222, Tianjin, China.

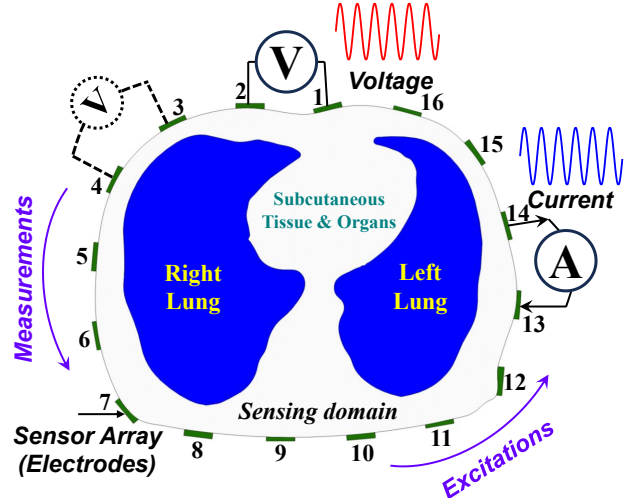


Fig. 1. The sensing principle of 16-electrode EIT system (taking lung measurement with chest shape as case).

The forward problem of EIT is to compute the voltage from the injection pattern and interior conductivity distribution, which can be modeled using the complete electrode model (CEM) [1], including the conductivity Laplace equation

$$\nabla \cdot (\sigma(x) \nabla u(x)) = 0, x \in \Omega \quad (1)$$

with corresponding boundary condition

$$\begin{aligned} u(x) + z_l \sigma(x) \frac{\partial u(x)}{\partial n} &= U_l, \quad x \in e_l, \quad l = 1, 2, \dots, L \\ \sigma(x) \frac{\partial u(x)}{\partial n} &= 0, \quad x \in \partial\Omega \setminus \bigcup_{l=1}^L e_l \\ \int_{e_l} \sigma(x) \frac{\partial u(x)}{\partial n} dS &= I_l, \quad l = 1, 2, \dots, L \end{aligned} \quad (2)$$

where  $n$  is the outward unit normal vector on the boundary,  $z_l$  is the contact impedances,  $I_l$  and  $U_l$  are the potential and current with respect to the electrode  $e_l$ . In addition, in order to ensure the existence and uniqueness of solution, the conservation of charge and potential of (2) is fixed as

$$\sum_{l=1}^L I_l = 0, \quad \sum_{l=1}^L U_l = 0 \quad (3)$$

The numerical solution to the forward model (1)-(3) is often obtained by using the finite element method (FEM), while considering the additive Gaussian noise  $\varepsilon$ , the observation model of EIT can be written as follows

$$\mathbf{V} = \mathcal{U}(\mathbf{x}; \mathbf{I}) + \varepsilon \quad (4)$$

where,  $\mathbf{V} \in \mathbb{R}^{L \times (L-3)}$  is the normalized measurement vector,

$\mathbf{x} \in \mathbb{R}^{m \times 1}$  is the discretized conductivity vector, and  $\mathcal{U}$  is the forward operator.

In this work, we mainly consider differential imaging to solve the EIT inverse problem. The aim of differential imaging is to reconstruct the conductivity variation at different states, i.e. estimating the  $\Delta\mathbf{x}$  at the time  $t_1$  (called reference state with the voltage  $V_1$  and conductivity  $\mathbf{x}_1$ ) and the time  $t_2$  (called measurement state with the voltage  $V_2$  and conductivity  $\mathbf{x}_2 = \mathbf{x}_1 + \Delta\mathbf{x}$ ). The reconstruction  $\Delta\mathbf{x}$  is expressed as the observation model using first-order Taylor approximation expressed as below:

$$\mathbf{V}_2(\mathbf{x}_1 + \Delta\mathbf{x}) \approx \mathbf{V}_1(\mathbf{x}_1) + \mathbf{A} \cdot \Delta\mathbf{x} + \boldsymbol{\varepsilon} \quad (5)$$

where,  $\mathbf{A} = \frac{\partial \mathcal{U}(\mathbf{x}_0)}{\partial \mathbf{x}}$  is the Jacobian (Sensitivity) matrix, and each element in this matrix is defined as  $A_{i,j} = -\int_{\Omega} \frac{\nabla \varphi_i}{I_i} \cdot \frac{\nabla \varphi_j}{I_j} d\Omega$  [2]. According to the Eq. (5), the mathematical model of differential imaging is  $\mathbf{V} = \mathbf{Ax} + \boldsymbol{\varepsilon}$ , where  $\mathbf{V}$  represents the differential values with normalization of  $\mathbf{V}_1$  and  $\mathbf{V}_2$ , and  $\mathbf{x}$  represents the  $\Delta\mathbf{x}$  conveniently. The inverse problem of EIT is often expressed as the following optimization problem

$$\mathbf{x}^* = \operatorname{argmin}_{\mathbf{x}} \left\{ \|\mathbf{V} - \mathbf{Ax}\|_2^2 + \lambda \mathcal{R}(\mathbf{x}) \right\} \quad (6)$$

Here,  $\mathcal{R}(\mathbf{x})$  denotes the regularization pattern.

### B. SDE-based EIT solver

Score-based diffusion gradually transforms data distributions into Gaussian distributions by injecting various Gaussian noise perturbations. The diffusion process  $\{\mathbf{x}(t)\}_{t=0}^T$  can be seen as the solution of the following SDE:

$$d\mathbf{x}_t = \mathbf{f}(\mathbf{x}_t, t) dt + g(t) d\mathbf{w}_t \quad (7)$$

where,  $t \in [0, T]$  is the continuous time variation,  $\mathbf{x}(0) = \mathbf{p}_0(\mathbf{x}_0 | \mathbf{y}) \sim p_{data}$ ,  $\mathbf{x}(t) = p_t(\mathbf{x}_t | \mathbf{y})$ ,  $\mathbf{x}(T) \sim p_T$  denotes the prior distribution.  $\mathbf{f}(\cdot, t)$  and  $g(t)$  are the drift and diffusion coefficients of  $\mathbf{x}(t)$ , and  $\mathbf{w}_t$  is the standard Wiener process. The reverse process is also a diffusion that the reverse-time SDE can model:

$$d\mathbf{x}_t = [\mathbf{f}(\mathbf{x}_t, t) - g^2(t) \nabla_{\mathbf{x}_t} \log p_t(\mathbf{x}_t | \mathbf{y})] dt + g(t) d\bar{\mathbf{w}}_t \quad (8)$$

where,  $\bar{\mathbf{w}}_t$  is the inversion of the standard Wiener process,  $\nabla_{\mathbf{x}_t} \log p_t(\mathbf{x}_t | \mathbf{y})$  denotes the score function that could be approximated using the score model  $s_{\theta^*}(\mathbf{x}_t, t)$  trained by

$$\theta^* = \operatorname{argmin}_{\theta} \mathbb{E}_{t \sim \mathcal{U}[0, T]} \left\{ \lambda_t \mathbb{E}_{\mathbf{x}(0)} \mathbb{E}_{\mathbf{x}(t) | \mathbf{x}(0)} \left[ \|s_{\theta}(\mathbf{x}(t), t; \mathbf{y}) - \nabla_{\mathbf{x}_t} \log p_{0|t}(\mathbf{x}(t) | \mathbf{x}(0), \mathbf{y})\|_2^2 \right] \right\} \quad (9)$$

Here,  $\lambda_t$  is the weight,  $p_{0|t}(\mathbf{x}(t) | \mathbf{x}(0), \mathbf{y})$  expresses the perturbation kernel. Once the score model  $s_{\theta^*}(\mathbf{x}_t, t)$  is trained by Eq. (9), the EIT image could be reconstructed by coupling the measured signal as:

$$\mathbf{x}_{t-\Delta t} = \mathbf{x}_t + g^2(t) s_{\theta^*}(\mathbf{x}_t, t; \mathbf{y}) + g(t) \sqrt{\Delta t} \cdot \mathbf{z} \quad (10)$$

### C. Schrödinger Bridge and I<sup>2</sup>SB

1) *Schrödinger Bridge*: SB is a nonlinear extension of score-based diffusion models, which defines the optimal

transportation between two arbitrary distributions. The forward/backward SDEs of SB are mathematically expressed as:

$$d\mathbf{x}_t = [\mathbf{f}_t + \beta_t \nabla \log \Psi(\mathbf{x}_t, t)] dt + \sqrt{\beta_t} d\mathbf{w}_t \quad (11)$$

$$d\hat{\mathbf{x}}_t = [\mathbf{f}_t + \beta_t \nabla \log \hat{\Psi}(\mathbf{x}_t, t)] dt + \sqrt{\beta_t} d\mathbf{w}_t \quad (12)$$

where,  $\mathbf{x}_0 \sim p_0$ ,  $\mathbf{x}_1 \sim p_1$  are boundary distributions in two distinct domains, and the functions  $\Psi(\cdot, t)$  and  $\hat{\Psi}(\cdot, t)$  are time-varying energy potentials that are determined by the following PDEs:

$$\begin{cases} \frac{\partial \Psi(\mathbf{x}_t, t)}{\partial t} = -\nabla \Psi^\top \mathbf{f}_t - \frac{1}{2} \beta_t \Delta \Psi \\ \frac{\partial \hat{\Psi}(\mathbf{x}_t, t)}{\partial t} = -\nabla \cdot (\Psi \mathbf{f}_t) + \frac{1}{2} \beta_t \Delta \hat{\Psi} \end{cases} \quad (13)$$

such that  $\Psi(\mathbf{x}_0, 0) \cdot \hat{\Psi}(\mathbf{x}_0, 0) = p_A(\mathbf{x}_0), \Psi(\mathbf{x}_1, 1) \cdot \hat{\Psi}(\mathbf{x}_1, 1) = p_B(\mathbf{x}_1)$ .

2) *Image-to-image SB (I<sup>2</sup>SB)*: The I<sup>2</sup>SB establishes diffusion paths between paired clean and degraded images. Let us define two distributions  $p_A(\mathbf{x}_0) = \delta(\mathbf{x}_0 - \mathbf{x}_{clean})$  and  $p_B(\mathbf{x}_1) = q_{init}$ , and set  $\mathbf{f}_t = 0$ , the forward diffusion of I<sup>2</sup>SB is designed to follow the Gaussian  $q(\mathbf{x}_t | \mathbf{x}_0, \mathbf{x}_1)$  as:

$$q(\mathbf{x}_t | \mathbf{x}_0, \mathbf{x}_1) = \mathcal{N} \left( \mathbf{x}_t; \frac{\bar{\sigma}_t^2}{\bar{\sigma}_t^2 + \sigma_t^2} \mathbf{x}_0 + \frac{\sigma_t^2}{\bar{\sigma}_t^2 + \sigma_t^2} \mathbf{x}_1, \frac{\bar{\sigma}_t^2 \sigma_t^2}{\bar{\sigma}_t^2 + \sigma_t^2} \mathbf{I} \right) \quad (14)$$

where,  $\sigma_t^2 = \int_0^t \beta_\tau d\tau$  and  $\bar{\sigma}_t^2 = \int_t^1 \beta_\tau d\tau$  represent accumulated variances from either side. The denoising network can be efficiently trained to predict the difference between  $\mathbf{x}_t$  and  $\mathbf{x}_0$  by the loss function

$$\theta^* = \operatorname{argmin}_{\theta} \mathbb{E}_{\mathbf{x}_0, \mathbf{x}_1} \mathbb{E}_{t, \mathbf{x}_t} \left[ \left\| \epsilon_{\theta}(\mathbf{x}_t, t) - \frac{\mathbf{x}_t - \mathbf{x}_0}{\sigma_t} \right\| \right] \quad (15)$$

In the generative stage, I<sup>2</sup>SB begins with the initial results  $\mathbf{x}_N$  and iteratively achieves the clean images  $\mathbf{x}_0$ . At the step from the  $\mathbf{x}_{t_n}$  to the  $\mathbf{x}_{t_{n-1}}$ , the expected mean of  $\mathbf{x}_0$  at the sampling time  $t_n$ ,  $\mathbf{x}_0^{(n)}$  is computed firstly based on the network, and the  $\mathbf{x}_{t_{n-1}}$  is sampled based on the DDPM posterior. This could be demonstrated as

$$\begin{cases} \mathbf{x}_0^{(n)} = \mathbf{x}_{t_n} - \sigma_n \epsilon_{\theta^*}(\mathbf{x}_{t_n}, t_n), \\ \mathbf{x}_{t_{n-1}} \sim p(\mathbf{x}_{t_{n-1}} | \mathbf{x}_0^{(n)}, \mathbf{x}_{t_n}) \\ = \mathcal{N} \left( \mathbf{x}_{t_{n-1}}, \frac{\alpha_{n-1}^2}{\sigma_n^2} \mathbf{x}_0^{(n)} + \frac{\sigma_{n-1}^2}{\sigma_n^2} \mathbf{x}_{t_n}, \frac{\alpha_{n-1}^2 \sigma_{n-1}^2}{\sigma_n^2} \mathbf{I} \right) \end{cases} \quad (16)$$

In Eq. (16),  $\alpha_{n-1}^2 = \int_{t_{n-1}}^{t_n} \beta_\tau d\tau$  denotes the accumulated variances between time steps  $t_{n-1}$  and  $t_n$ .

## II. DETAILS OF TRAINING DATASETS

In this section, we provide more detailed information of the simulation training datasets.

The observation area is set a circular shape with the diameter of 0.19 m, and there are 16 electrodes uniformly attached on the outside boundary of the domain. The protocol of data acquisition is ‘adjacent current excitation-adjacent voltage measurement’, where the current is utilized with the amplitude of 4.5 mA and the frequency of 50kHz. The NaCl solution with 0.06 S/m is set up as background in the homogeneous field.

1) *Multiphase conductivities with complicated shapes*: One to four circular inclusions with random position are simulated in database. The shapes of the inclusions include

squares, triangles, and circles. There are also some mixtures of all three shaped inclusions. Among them, the squares and triangles having different angles of rotation and the inclusions not overlapping each other. The radius is set as the range of 0.02–0.08m, and inclusions do not intersect each other. The mediums are set to a different conductivity, whose value are in the range of  $10^{-6}$  to  $10^6$  S/m. A total of 52,430 simulation samples are obtained. The training, validation and test samples are set to be 80%, 10% and 10% of the total database respectively.

2) *Healthy/injured lung-phantom datasets:* The procedure of lung-shaped data mainly includes four steps: CT image selection, lung region segmentation, lung shape establishment, and model augmentation. The lung CT images are selected from the Lung Image Database Consortium image collection (LIDC-IDRI) provided by the Cancer Imaging Archive (TCIA). Eighty patients from the database are selected and randomly divided into two groups, in which the chest CT images of 70 patients are used as training samples and the CT images of the remaining 10 patients are used as test samples. For each patient, we only study the CT slices within 8-cm vertical distance to the central slice, which leads to 350 and 50 slices in the training and testing data sets, respectively. The global thresholding image segmentation algorithm is applied to extract the lung contours. The approximate conductivity parameters for the internal organs (subcutaneous tissue, lungs, heart/aorta and spine) are set to the Table I. The lung injury is simulated by randomly removing a portion of the lungs and replacing the missing portion with the other medium, where the conductivity of the injured lungs ranged from 0.165 to 0.285 S/m. For augmenting the simulation data, the Gaussian white noise is added into the measurements with a signal-to-noise ratio (SNR) of 65 dB. Finally, the number of simulated lung phantoms is 9,100 for training and 1,000 for testing, respectively.

TABLE I  
CONDUCTIVITY VALUES OF DIFFERENT ORGANS IN THE HUMAN CHEST.

Organs	Fat	Lung	Heart	Aorta	Spine
Conductivity	0.30	0.15	0.50	0.60	0.09

### III. COMPLEMENTARY RESULTS

In this section, we provide more experimental results, including the *in-distribution measurements with real-world tank phantoms* as well as the *out-of-distribution data with KTC-2023 statical settings and chest-shape domain dynamic scenarios*.

#### A. Reconstruction results of tank phantom

In this subsection, there are including three real-world experiments with tank phantoms. The first case is the multiphase inclusions with various shapes and the second case is the lung-shape phantoms with ‘healthy/injured’ parts. The compared methods are CycleGAN, CSD\*, CD-EIT, CDMVC, DDRM, DDNM, DDS, I<sup>2</sup>SB, CDDB, SDB, and our D<sup>2</sup>PC-EIT, where the model configuration is illustrated in sub-section III-B of the main paper. In these results, we give the reconstruction results, the enlarged zoom of ROI and the absolute error map are

TABLE II  
THE QUANTITATIVE METRICS (RMSE, PSNR, AND SSIM) OF OUT-OF-DISTRIBUTION TEST 1: KTC-2023 PUBLIC BENCHMARK. THE DATA PRESENTATION IS MEAN  $\pm$  STD, AND THE COMPETING METHODS ARE CYCLEGAN, CSD\*, CD-EIT, CDMVC, DDRM, DDNM, DDS, I<sup>2</sup>SB, CDDB, SDB, AND OUR D<sup>2</sup>PC-EIT.

	RMSE	PSNR	SSIM
CycleGAN	23.392 $\pm$ 6.494	22.368 $\pm$ 2.450	0.859 $\pm$ 0.035
CSD*	18.047 $\pm$ 4.999	24.611 $\pm$ 2.393	0.887 $\pm$ 0.028
CDEIT	14.043 $\pm$ 4.120	26.809 $\pm$ 2.469	0.907 $\pm$ 0.022
CDMVC	11.636 $\pm$ 3.178	28.442 $\pm$ 2.493	0.920 $\pm$ 0.019
DDRMM	9.626 $\pm$ 2.587	30.088 $\pm$ 2.431	0.931 $\pm$ 0.016
DDNM	8.462 $\pm$ 2.180	31.213 $\pm$ 2.412	0.939 $\pm$ 0.014
DDS	7.528 $\pm$ 2.011	32.250 $\pm$ 2.463	0.945 $\pm$ 0.013
I <sup>2</sup> SB	6.701 $\pm$ 1.810	33.272 $\pm$ 2.436	0.951 $\pm$ 0.011
CDDB	6.102 $\pm$ 1.565	34.084 $\pm$ 2.435	0.955 $\pm$ 0.010
SDB	5.615 $\pm$ 1.659	34.873 $\pm$ 2.556	0.959 $\pm$ 0.010
D <sup>2</sup> PC-EIT	3.501 $\pm$ 0.727	38.665 $\pm$ 1.787	0.978 $\pm$ 0.002

TABLE III  
THE QUANTITATIVE METRICS (RMSE, PSNR, AND SSIM) OF OUT-OF-DISTRIBUTION TEST 2: DYNAMIC SCENARIO WITH CHEST-SHAPE TANK PHANTOM. THE DATA PRESENTATION IS MEAN  $\pm$  STD, AND THE COMPETING METHODS ARE CYCLEGAN, CSD\*, CD-EIT, CDMVC, DDRM, DDNM, DDS, I<sup>2</sup>SB, CDDB, SDB, AND OUR D<sup>2</sup>PC-EIT.

	RMSE	PSNR	SSIM
CycleGAN	30.186 $\pm$ 8.480	15.046 $\pm$ 2.267	0.847 $\pm$ 0.079
CSD*	24.153 $\pm$ 7.039	16.707 $\pm$ 2.223	0.885 $\pm$ 0.060
CDEIT	17.139 $\pm$ 6.362	17.584 $\pm$ 2.231	0.902 $\pm$ 0.055
CDMVC	15.123 $\pm$ 5.325	18.641 $\pm$ 2.204	0.919 $\pm$ 0.048
DDRMM	12.102 $\pm$ 4.026	16.994 $\pm$ 2.231	0.941 $\pm$ 0.035
DDNM	10.098 $\pm$ 5.027	20.562 $\pm$ 2.189	0.944 $\pm$ 0.038
DDS	9.090 $\pm$ 3.925	21.318 $\pm$ 2.240	0.952 $\pm$ 0.031
I <sup>2</sup> SB	7.082 $\pm$ 3.022	22.146 $\pm$ 2.191	0.960 $\pm$ 0.025
CDDB	5.078 $\pm$ 2.521	22.583 $\pm$ 2.189	0.964 $\pm$ 0.023
SDB	5.073 $\pm$ 2.019	23.174 $\pm$ 2.175	0.968 $\pm$ 0.020
D <sup>2</sup> PC-EIT	4.357 $\pm$ 1.414	25.296 $\pm$ 2.165	0.981 $\pm$ 0.010

also given for illustrating the performance. The analysis of the reconstructions between our D<sup>2</sup>PC-EIT and other competing methods could refer to the main paper. The reconstruction results are shown in Figure 2, where we show the reconstructed images, enlarged zoom images of ROI area, and the absolute error map between the ground truth and the reconstruction in each test case.

#### B. Reconstruction results of Out-of-distribution data

This section presents experimental results for two sets of out-of-distribution data: the publicly benchmark simulation dataset KTC2023 and dynamic experiments using a tank phantom with chest-shape domain. Specifically: (1) To increase reconstruction difficulty, we utilized the open-source KTC2023 shapes of inclusions while assigning multiple conductivities to different objects. This approach thoroughly validates the advantages of our proposed D<sup>2</sup>PC-EIT method over competing methods in reconstructing both shape and parameters. (2) The dynamic experiment simulating the observation domain with chest shape replicates the dynamic respiratory process involving ‘injured’ regions. In this experiment, physiological saline

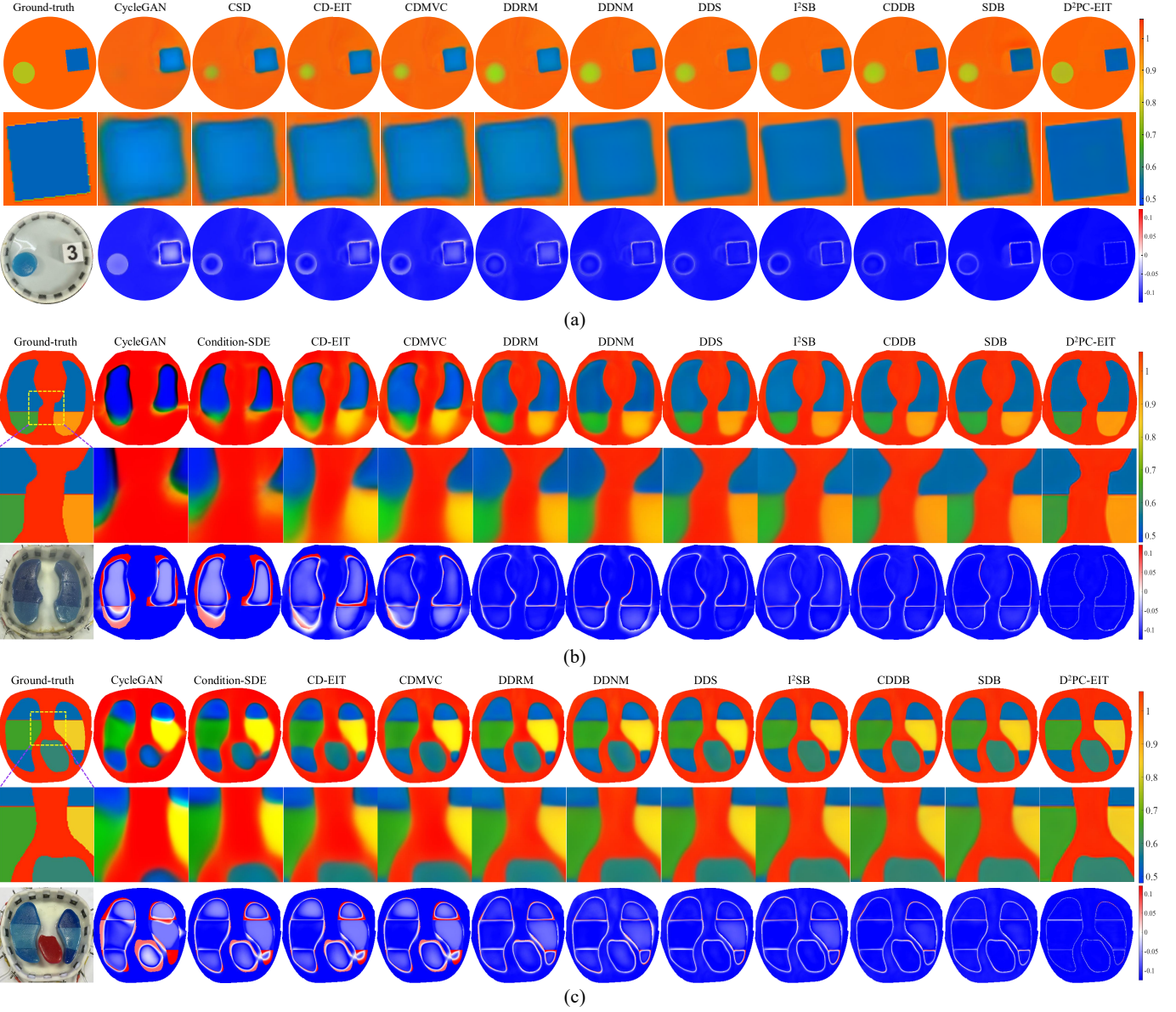


Fig. 2. The reconstruction results of statical setting with real-world tank phantoms (reconstructed conductivity distribution, enlarged zoom image of region-of-interest (ROI), and absolute error map). The first row shows, from left to right, the ground truth and the reconstructions of the various comparison methods, including CycleGAN, CSD\*, CD-EIT, CDMVC, DDRM, DDNM, DDS,  $I^2$ SB, CDDB, SDB, and our  $D^2$ PC-EIT. The second row shows the enlarged view of the ROI shape performance framed by the dot-line box. The third row shows the absolute error map between the reconstructions and the ground truth, where these maps are displayed ranging [0, 1].

was first injected into a designated ‘healthy’ region to increase conductivity, followed by an equal volume of distilled water injected at the same rate to decrease conductivity. Throughout this process, the conductivity of the ‘injured’ region is unchanged. This experimental setup simulates diseases such as pulmonary effusion and pneumonia. The reconstruction results from the out-of-distribution experiments are shown in Figures 3 and 4. In these results, the Figure 3 is the reconstructions of KTC-2023 public benchmark, where each result includes the reconstructed images, enlarged zoom images of ROI area, and the absolute error map between the ground truth and the reconstruction, and Figure 4 shows the reconstructions of dynamic phantom experiment with chest-shape domain, where the result is composed of reconstructions of one frame, and

the  $x - t/y - t$  image as well as the corresponding absolute error map of  $x - t/y - t$  image. The corresponding metrics, RMSE, PSNR, and SSIM, are given in Tables II and III.

We have the following insights from the abovementioned reconstructions: The visualizations and metrics reveal that a single random degradation in the image domain, achieved through forward diffusion and reverse generation, results in noticeable distortion in the reconstructions. These unsatisfactory results occur because of ignoring the constraints of measurement consistency. The SB-based methods realize deterministic modeling and utilize the initial prior as conditions to guide the generative process. Nevertheless, this approach is susceptible to instability in final results caused by errors in initial reconstructions. Our  $D^2$ PC-EIT introduces deterministic

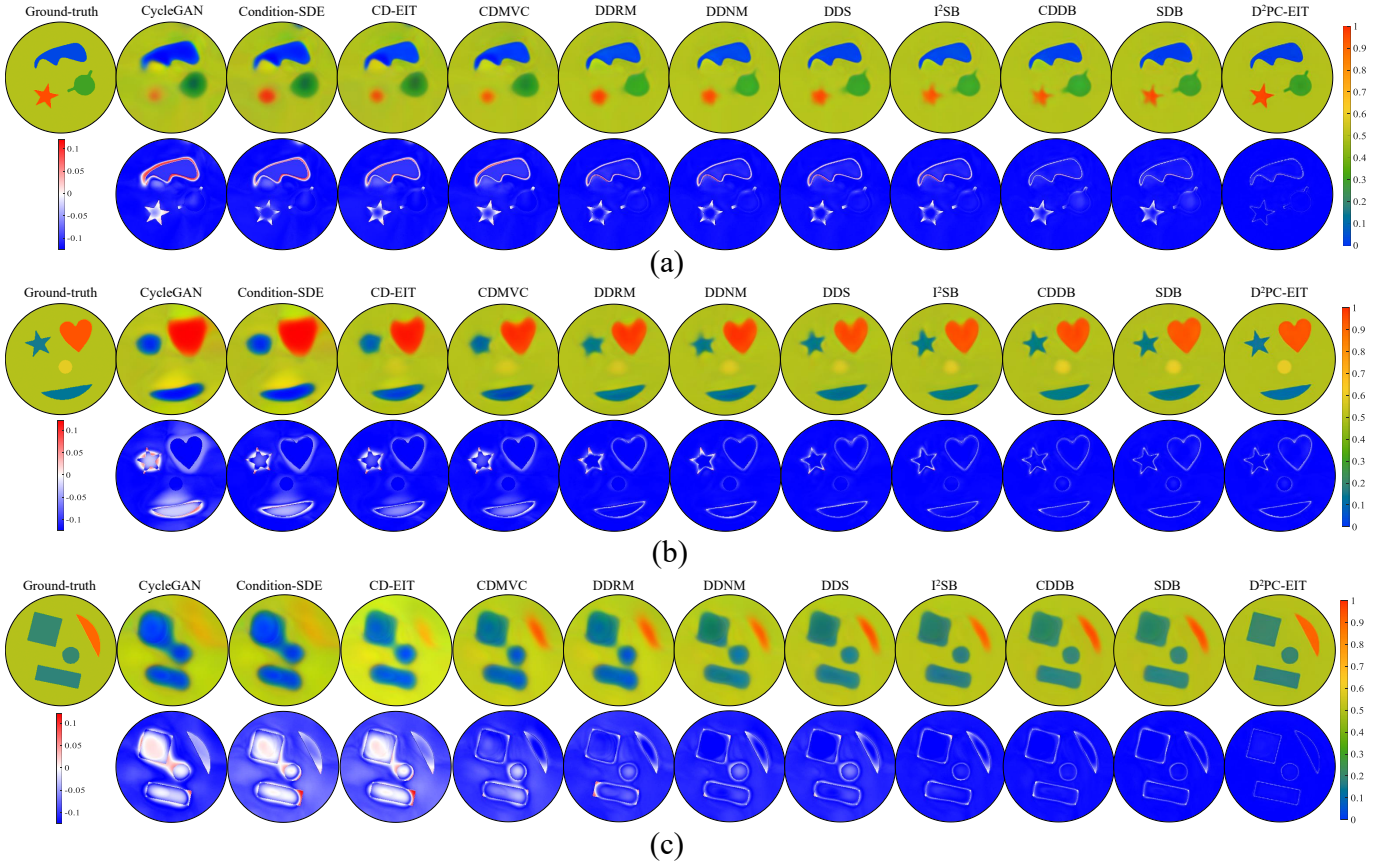


Fig. 3. The reconstruction results of Out-of-distribution test data of KTC-2023. The reconstructed results are obtained by different methods, including CycleGAN, CSD\*, CD-EIT, CDMVC, DDRM, DDNM, DDS,  $I^2$ SB, CDDB, SDB, and our  $D^2$ PC-EIT. The first row shows, from left to right, the ground truth and the reconstructions of the various comparison methods, and the third row shows the absolute error map between the reconstructions and the ground truth, where these maps are displayed ranging [0, 1].

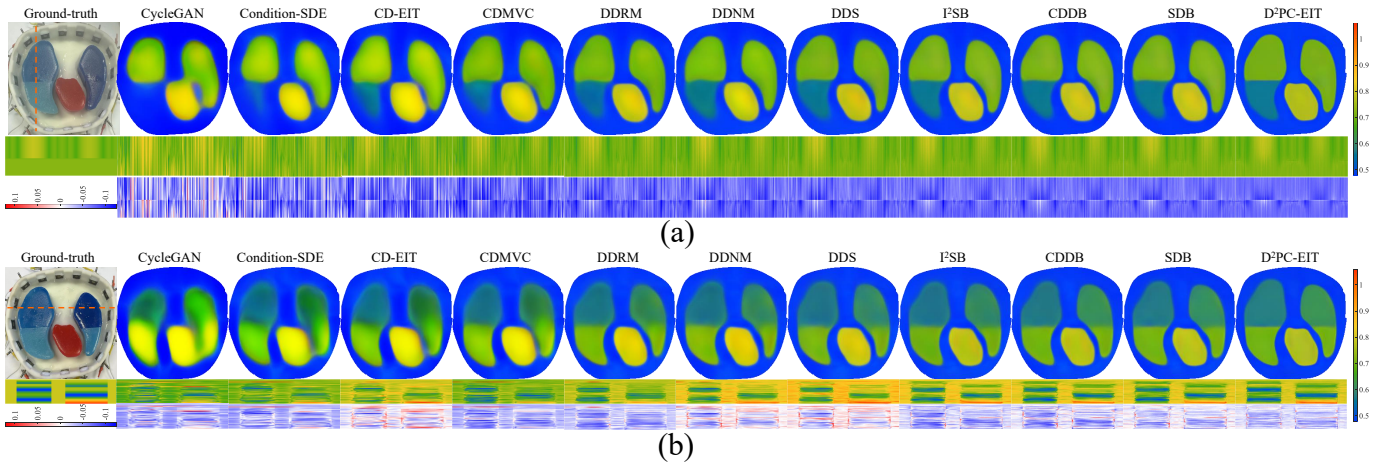


Fig. 4. The reconstruction results of Out-of-distribution test data with dynamic scenarios under the chest-shape tank phantom, which includes the reconstructed images of one frame, the  $x-t/y-t$  image of conductivity changes, and the corresponded absolute error map of  $x-t/y-t$  image. The first row shows, from left to right, the ground truth and the reconstructions of the various comparison methods, including CycleGAN, CSD\*, CD-EIT, CDMVC, DDRM, DDNM, DDS,  $I^2$ SB, CDDB, SDB, and our  $D^2$ PC-EIT. The  $x-t/y-t$  image (extraction of the 65-th (Case (a)) and 70-th (Case (b)) along the  $x/y$  and temporal dimensions, as marked by the yellow dotted line) and the error of  $x-t/y-t$  image are also shown to illustrate the reconstruction performance in the temporal dimension.

$cl^3$ SB modeling and stochastic PiCs guided sampling, as well as incorporating bidirectional physics correction using the INN framework. This method ensures the framework of the inverse solver aligns with the forward observation model, while introducing two distinct sampling processes that are

interacting with each other. Therefore, the reconstructions show ideal spatial and time resolution and have better measurement consistency. In addition, the results show similar performances on both in-distribution and out-of-distribution data, demonstrating that our method has robust generalization.

#### IV. RELATED WORKS

This section reviews the related works from the following aspects, including the EIT reconstruction methods with learning-based frameworks, the diffusion-based methods for solving inverse imaging problems, and the Schrödinger Bridge (SB)-based methods in computer vision tasks. Finally, we summarize the main distinctions between our D<sup>2</sup>PC-EIT and the related works.

##### A. Learning-based frameworks for EIT

Currently, the learning-based frameworks with supervised manner for EIT reconstruction can be categorized into two types. The first idea employs the ‘end-to-end’ framework, with image-driven idea, which achieves the high-quality imaging results with fewer artifacts. The second idea utilizes the model-driven unrolling framework combined with physical priors to improve the nonlinear representation, clear, and generalization capability. Further, the unsupervised manner for EIT inverse problem solver are increasingly being researched and applied.

1) *Image-driven ‘end-to-end’ framework:* Since the introduction of the U-Net [3], several methods with convolutional neural networks (CNNs) have extended the standard U-shape architecture to achieve high-quality image reconstruction. This approach typically employs sensitivity-based numerical solutions to obtain ‘coarse’ initial images, followed by denoising or enhancement of specific artifacts using U-shaped CNNs to obtain ‘fine’ reconstructions. S. J. Hamilton et al. [4] propose the Deep D-Bar, which utilizes U-Net to filter the oversmooth distortion of lung shapes caused by truncated low-pass filtering in the D-Bar. Similarly, Cen et al. [5] introduced the Deep Calderón method, employing U-Net to construct a nonlinear mapping between initial ‘coarse’ images and high-quality ‘fine’ reconstructions. Tian et al. [6] proposed a residual U-Net with dilated convolutions to address the limitation of central fields being insensitive to excitation signals. Ren et al. [7] introduced a two-stage deep learning (TSDL) reconstruction method, which uses the shape of the observation domain as prior to guide a dual-branch residual network, as well as enhancing the robustness of reconstruction results. AymanAameen et al. [8] proposed TSS-ConvNet, employing a convolutional interaction operator with three branches, spatial, spectral, and truncated spectral, to enhance global and local feature for EIT image reconstruction. Fu et al. [9] introduced SFCF-Net, which explores multi-path dense connections to establish frequency-domain correlations for multi-frequency EIT (mfEIT). Wang et al. [10] designed the DELTA, which considers dual-branch Encoder comprising CNN and Transformer to learn local features and global information within the observation field, in order to achieve high-resolution EIT image reconstruction. Xiao et al. [11] integrated the KAN into the U-Net architecture, enabling more precise mapping of boundary voltages to conductivity variations. This approach demonstrated significant potential for enhancing the accuracy and robustness of three-dimensional conductivity distribution reconstruction, such as TTfield monitoring.

2) *Model-driven unrolling architecture:* The unrolling-based neural architectures embeds the learnable NNs into the iterative optimization algorithms for obtaining the model parameters and adaptive regularization patterns [12]. Due to incorporate physic priors as conditions, this kind of methods

exhibit superior generalization and interpretability. William Herzberg et al. [13] proposed GCNM, which embeds FEM-based forward operators into the inverse problem solving framework and leveraging graph structures to enhance the flexible structural representation. Xiang et al. [14] introduced FISTA-Net, an unrolling network based on the FISTA algorithm that learns soft-thresholding operators for EMT and LdCT imaging. Francesco et al. [15] developed the EITGN-Net unrolling framework, which integrates the anisotropic total variation (TV) function as attention-like module within a Gaussian-Newton iterative framework to deliver robust and high-quality reconstructions. Dong et al. [16] proposed the SWISTA-Net method based on wavelet-domain decomposition, where this method utilizes various subband frequencies to enhance prior representation and achieve high-quality detail enhancement. Ma et al. [17] introduced PDCISTA-Net employing dual CNNs to model multi-scale features, which proved effective for tactile sensing in EIT. Zhou et al. [18] introduced LPGD-RMA and LPD-RMA unrolling frameworks by incorporating LSTM-based strategies to achieve recurrent momentum acceleration (RMA), demonstrating their effectiveness in solving nonlinear inverse problems. Furthermore, they [19] also proposed the learnable semi-quadratic splitting network (HQSNNet) with Anderson acceleration, referred as to AA-HQSNNet, achieving significantly faster convergence and substantial artifact suppression. Yang et al. [20] explored the MMV-Net based on ADMM framework for mfEIT, which employs the spatial self-attention module and the convolution-LSTM block to learn spatial and frequency correlations, respectively. Wang et al. [21] proposed the RwTVSB-Net, which unrolls the Split Bregman algorithm with reweighted TV regularization. This architecture introduces the deformable convolutions and large-kernel convolutions for representing the multi-scale latent features and adaptive nonlinear soft-thresholding operator.

3) *Unsupervised manner for EIT imaging:* In recent years, unsupervised methods have been widely applied to inverse problem solving due to their requirement-free large amounts of paired datasets. Currently, unsupervised EIT image reconstruction can be primarily categorized into two types: deep image priors (DIP)-based methods and generation-based methods. The DIP-based prior methods could adaptively learn latent prior in the image domain, where these explicit priors have been proved that is the core challenge of designing flexible regularizations [22]. Liu et al. [23] first introduced the DIP strategy, referred as to DeepEIT, into EIT image reconstruction. The DeepEIT method can also be extended with other prior presentations in order to further improve the reconstructions. Subsequently, Liu et al. [24] proposed a coordinate-information-based DIP reconstruction method, which maps input coordinates to Fourier features with adjustable bandwidth, enabling the multi-layer perceptron (MLP) to capture rich high-frequency information. Next, Shan et al. [25] developed the GraphEIT, which combines implicit feature representation via INR-based network based on graph networks. The GraphEIT not only enhances the fidelity of reconstructed images but also ensures robustness against the inherent challenges of irregular-domain inverse problems. Xia et al. [26] employed heuristic networks with the NAS strategy, which aims to design a U-shaped DIP architecture for enabling the Encoder to efficiently acquire rich tomographic features.

Yang et al. [27] proposed R-SIP method based on shallow neural network for constructing the image-domain prior, which serves as the regularization pattern for 3D-EIT reconstruction. Wang et al. [28] introduced a novel approach to enhance EIT image reconstruction performance by employing a deep prior strategy empowered by semantic latent embedding, which maximizes the utilization of prior information learned from reference images. The generation model for EIT solver typically starts from random noise and progressively remove it to reconstruct high-quality images. Moreover, the measurement-domain information or initial ‘coarse’ reconstruction are simultaneously incorporated as the guided condition to optimize the sampling process. For example, Xiong et al. [29] proposed the DiffusionEIT, where the measured voltage is the condition in the sampling as well as the Transformer-based denoising network is designed to fuse the condition and image to control the generation process. Similarly, Shi et al. [30] introduced the CDEIT, which directly conditions the probability distribution of conductivity distributions on boundary voltages in an end-to-end manner. Liu et al. [31] proposed CDMVC that implements voltage consistency during the sampling stage using a pre-trained forward problem solver network. This approach incorporates physical prior based on the EIT observation model to enhance imaging quality. Zhou et al. [32] introduced a conditional SDE diffusion (CSD) model. Unlike the original SDE-based diffusion that samples from random noise, CSD starts from initial reconstructions based on Gauss-Newton iterations to incorporate additional prior within the image domain.

Overall, we have the following insights according to the aforementioned previous work: The existing EIT reconstruction methods with supervised manner requires a large number of high-quality paired training samples. The performances of these supervised models depends on the quality and distribution of the training samples, which significantly limits the generalization. Although the DIP-based methods with unsupervised manner do not require training, this kind of method significantly increase computational resource and reconstruction time, due to they necessitate incorporating FEM-based solvers into the optimization process. In addition, the diffusion-based reconstruction methods performs noise perturbation and denoising processes solely within the image domain. While measurement conditions participate in reverse sampling as auxiliary guidance, this kind method ignores the observation model and inherent physical constraints of EIT. Therefore, the reconstructions obtained by diffusion ideas usually show obvious uncertainty.

### B. Diffusion-based solvers for inverse problems

Diffusion-based methods have obtained significant attention in inverse problem solving due to the powerful generative capabilities, particularly excelling in producing high-quality, diverse samples with complex textures. This section reviews two inverse problem solving tasks: low-level vision and tomography reconstruction.

*1) Low-level vision:* Diffusion models primarily focus on restoring corrupted data. The aim is to reconstruct high-quality images with detailed semantics and realistic textures, even in severely and complexly degraded scenarios [33], [34]. Zeng et al. [35] proposed an image enhancement framework based on the Laplace domain, which comprises the

ADALE abnd PUHE two core blocks to realize high-quality underwater image enhancement. Yu et al. [36] proposed a diffusion-based decoupled degradation representation method, referred as to D3BSR, for bind image SR task. This method decomposes arbitrary unknown degradations into structural and textural degradations to enhance perceptual and fidelity quality, respectively. Qing et al. [37] proposed the DiffUIE, which firstly introduces a global feature prior to enhance the representation of the diffusion model. Simultaneously, it incorporates an underwater image degradation model to facilitate ‘detail’ learning between high-quality and degraded images. Hu et al. [38] designed the ICDSR, that utilizing low-resolution images as guiding conditions while incorporating a multi-scale denoising network, to achieve single-image super-resolution. Wang et al. [39] proposed the LPCDiff based on the Laplace pyramid architecture. This approach captures multi-frequency features within images without increasing inference complexity, achieving satisfactory results in real-world image dehazing. Huang et al. [40] addressed the long inference time of diffusion models by proposing the WaveDM. By leveraging the sparse properties of the wavelet domain and an efficient conditional sampling strategy, it achieved favorable results across multiple image restoration tasks. Zhao et al. [41] introduced diffusion models into the frequency domain and proposing a frequency-condition low-light image enhancement method. This approach enhances high-frequency details within low-light images by adaptively learning k-sparse high-frequency features. Luo et al. [42] proposed the HDiff-HIR, which designed a mask-condition generation module to incorporate measurement data into the denoising network. They also developed a global-local attention mechanism, LGS-MSA, to efficiently construct complex feature dependencies. Xie et al. [43] introduced Reffusion, which employs a dual-domain interactive Transformer in both spatial and wavelet domains, achieving promising results across multiple image restoration tasks. Liu et al. [44] proposed the IM-Diff, which designed a reference-image-based cross-Mamba (RCM) and a nonlinear characteristic of wavelet implicit neural networks to achieve implicit continuous representation learning at arbitrary scales. Zhang et al. [45] proposed a novel texture-preserving diffusion model for CBCT-to-CT synthesis. This method effectively enhances detail preservation in synthesized images through adaptive optimization of high-frequency texture details and cross-modal feature interaction between CBCT and CT.

*2) Tomography reconstruction:* The key advantages of diffusion methods include advanced image distribution modeling, improved robustness to domain shifts, and principled quantification of reconstruction uncertainty. These superiorities effectively mitigate the limitations of lacking high-quality paired training data in tomography imaging tasks [46]. This sub-section mainly reviews three tasks, including the low-dose CT (LdCT), CS-based accelerated MR reconstruction (CS-MRI), and sparse-view photoacoustic tomography (PAT).

*(a) LdCT imaging:* Wu et al. [47] proposed the model-guided stable diffusion (MISD), which addresses the impact of noise and limited data on fractional generation models by establishing a noise model using physical priors in the sinogram. Shan et al. [48] proposed the noise-inspired enhanced diffusion (NEED) for universal LdCT reconstruction. This approach accounts for the inherent Poisson noise bias in measurement data, while the dual-guided diffusion framework

enhances structural prior localization to improve reconstruction quality. Liu et al. [49] designed the sinusoidal wavelet random decomposition-based random mask (SWARM) diffusion model. By employing a random masking strategy to augment the training sample space, this approach enhances the feature representation capability, uncertainty quantitative, generalization performance, and detail preservation. Wu et al. [50] designed a fractional generation model in the measurement domain. It trained a fractional model utilizing measurements with full-dose scans to obtain prior information, then iteratively executes an SDE solver and data consistency term to acquire full-dose measurement information. This method improved the quality of FBP-based reconstruction. Yu et al. [51] proposed residual Poisson flow (ResPF) based on the Poisson flow generative model (PFGM). This innovative design incorporates a skip-sampling hijacking strategy to enhance sampling efficiency while introducing a residual fusion that combines image-domain and physical-prior information to improve reconstruction consistency.

(b) **CS-MRI**: Jong et al. [52] pioneered the application of SDE-based diffusion models for accelerated MR imaging, comprehensively addressing reconstruction schemes for real-valued MRI, complex-valued MRI, and various acceleration modes using VP-SDE and VE-SDE frameworks. Liang et al. [53] introduced a time-cross K-space acquisition strategy, which employed a two-stage diffusion model to learn global-local prior and enabled zero-sample dynamic MR. Gyutaek et al. [54] proposed an annealing fractional diffusion model for motion artifact removal in MR images. It trains solely on motion-free fractional models and then iteratively employs forward and reverse diffusion processes to eliminate motion artifacts. Zhu et al. [55] proposed the high-frequency space SDE-based diffusion (HFS-SDE), which employs forward noise perturbation and reverse denoising only in the high-frequency K-space while preserving low-frequency K-space information. This approach enhances detail reconstruction in the high-frequency domain while accelerating the speed of reverse sampling. Sun et al. [56] proposed the progressive reconstruction and denoising diffusion model (PRDDiff) for arbitrary-scale MR SR. It achieves continuous resolution enhancement by designing an adaptive resolution recovery network (ARRNet) and a multi-stage SR strategy.

(c) **Sparse-view PAT**: Ma et al. [57] proposed diffusion-based sparse tomography angle recovery (D-STAR), which significantly reduced the number of angles required for high-resolution PAT while maintaining image quality comparable to full-angle imaging. Song et al. [58] proposed a sinogram-domain spectral reconstruction for the enhanced fractional diffusion model (ESDM), which learns cross-scale dependencies between full-bandwidth and finite-bandwidth sinograms to enhance the prior guidance of the reconstruction method. Liu et al. [59] proposed a multi-diffusion-enhanced reconstruction strategy that alternates forward and reverse diffusion processes to generate sparse measurement data, thereby improving reconstruction quality. Sreemanti et al. [60] introduced a conditional fractional diffusion model for sparse PAT reconstruction, incorporating expressive prior information learned from the diffusion model into the reverse solver to enhance reconstruction quality. Li et al. [61] proposed a model-driven and diffusion-prior-driven ultra-sparse PAT method. This approach completes sinogram information through a reverse diffusion

process, thereby incorporating the generative prior from the diffusion model as a constraint in the optimization problem to improve reconstruction quality.

The abovementioned low-level vision tasks and tomography reconstruction tasks benefit from diffusion-based generation methods. However, these methods can not be applied to solving EIT reconstruction directly: On one hand, diffusion models designed for low-level vision tasks do not need to consider sophisticated mappings between measurement domains and image domains, achieving satisfactory reconstruction results by fully leveraging image-domain information. On the other hand, existing reconstructions such as LdCT, MRI, and PAT, as well as EIT inverse problems, exhibit significant differences in physical formulation and observation models. Therefore, it is significant to design diffusion models based on the physical mechanisms and observation models of specific EIT task.

### C. Schrödinger Bridge-based Solvers and distinctions

Compared to diffusion-based methods, such as DDPM and SDE, the Schrödinger Bridge (SB)-based method can construct optimal transportation between any two distributions, which is not limited to generating images starting from Gaussian distributions. In recent years, some studies have introduced the SB method-based methods into inverse problem solving. Herman et al. [62] first proposed combining deep unrolling with the Direct SB (DSB) to integrate physical information into the network, thereby facilitating the transition from degraded images to high-quality images with fewer sampling steps. Mirza et al. [63] addressed image degradation stemming from discrepancies between the asymptotic normality assumed in diffusion priors and the learned transformation. They designed the Fourier-constrained diffusion bridge (FDB), which enables transformation between the undersampled data and the fully sampled data. Wu et al. incorporated measurement information as guided conditions into the SB sampling, which designed the measurement-embedded SB (MESB) [64], projection-embedded SB (PESB) [65], and system matrix embedded Schrödinger Bridge (SDB) [66]. These methods naturally incorporate data consistency into the diffusion process to implement physical constraints, also enhancing the quality of reconstructions. Hu et al. [67] proposed the adaptive diffusion bridge for inverse problems (ADOBII) to solve blind inverse problems with unknown forward models. This approach adaptively calibrates the unknown forward observation model to enforce data consistency constraints.

The aforementioned SB-based methods for solving inverse problems typically employ forward models to enforce data consistency hard constraints. However, these approaches cannot be directly applied to tasks with explicit nonlinear characteristics, such as the EIT inverse problem. From these review of previous learning-based EIT reconstruction methods, we can conclude that the main differences between D<sup>2</sup>PC-EIT and the competing methods:

(1) Our proposed D<sup>2</sup>PC-EIT carefully designs a dual-branch diffusion framework, which fully incorporates both deterministic degradation with SB optimal transportation as well as stochastic degradation with PiCs. These two architectures describe distinct mechanisms in the forward process, which is comprehensively constructing the nonlinearity and ill-posedness of EIT inverse problem.

(2) In the D<sup>2</sup>PC-EIT, we designs the forward operators and inverse mappings with INN-based framework. This PC architecture could leverage the nonlinear characteristic of NNs to introduce data consistency, as well as avoid the accumulation of linear-sensitivity errors caused by measurement consistency constraints.

(3) Unlike existing diffusion-based image reconstruction methods, our designed D<sup>2</sup>PC-EIT employs a data-flow process consistent with the forward observation model. By utilizing a well-posed forward problem to implement condition-guide of physical priors and data consistency constraints, it significantly reduces the uncertainty in reconstructions.

## REFERENCES

- [1] E. Somersalo, M. Cheney, and D. Isaacson, "Existence and uniqueness for electrode models for electric current computed tomography," *SIAM Journal on Applied Mathematics*, vol. 52, no. 4, pp. 1023–1040, 1992.
- [2] T. Zhang, Z. Wang, and Q. Wang, "A sensitivity prior generation with conditional diffusion model for eit reconstruction," *IEEE Signal Processing Letters*, vol. 32, pp. 3042–3046, 2025.
- [3] R. Azad, E. K. Aghdam, A. Rauland, Y. Jia, A. H. Avval, A. Bozorgpour, S. Karimijafarbigloo, J. P. Cohen, E. Adeli, and D. Merhof, "Medical image segmentation review: The success of u-net," *IEEE Transactions on Pattern Analysis and Machine Intelligence*, vol. 46, no. 12, pp. 10 076–10 095, 2024.
- [4] S. J. Hamilton and A. Hauptmann, "Deep d-bar: Real-time electrical impedance tomography imaging with deep neural networks," *IEEE Transactions on Medical Imaging*, vol. 37, no. 10, pp. 2367–2377, 2018.
- [5] S. Cen, B. Jin, K. Shin, and Z. Zhou, "Electrical impedance tomography with deep calderón method," *Journal of Computational Physics*, vol. 493, p. 112427, 2023.
- [6] X. Tian, X. Liu, T. Zhang, J. Ye, W. Zhang, L. Zhang, X. Shi, F. Fu, Z. Li, and C. Xu, "Effective electrical impedance tomography based on enhanced encoder-decoder using atrous spatial pyramid pooling module," *IEEE Journal of Biomedical and Health Informatics*, vol. 27, no. 7, pp. 3282–3291, 2023.
- [7] S. Ren, K. Sun, C. Tan, and F. Dong, "A two-stage deep learning method for robust shape reconstruction with electrical impedance tomography," *IEEE Transactions on Instrumentation and Measurement*, vol. 69, no. 7, pp. 4887–4897, 2020.
- [8] A. A. Ameen, A. Sack, and T. Pöschel, "Tss-convnet for electrical impedance tomography image reconstruction," *Physiological Measurement*, vol. 45, no. 4, p. 045006, 2024.
- [9] X. Tian, J. Ye, T. Zhang, L. Zhang, X. Liu, F. Fu, X. Shi, and C. Xu, "Multi-path fusion in sfcf-net for enhanced multi-frequency electrical impedance tomography," *IEEE Transactions on Medical Imaging*, vol. 43, no. 8, pp. 2814–2824, 2024.
- [10] Z. Wang, T. Zhang, and Q. Wang, "Delta: Delving into high-quality reconstruction for electrical impedance tomography," *IEEE Sensors Journal*, vol. 25, no. 8, pp. 13 618–13 631, 2025.
- [11] Y. Xiao, L. Wang, C. Chen, S. Hu, M. Lu, H. Yu, and J. C. Rajapakse, "Integrating kolmogorov-arnold network and unet architecture for reconstruction of 3-d electrical impedance tomography to assess the efficacy of tumor treating fields," *IEEE Transactions on Instrumentation and Measurement*, vol. 74, pp. 1–10, 2025.
- [12] V. Monga, Y. Li, and Y. C. Eldar, "Algorithm unrolling: Interpretable, efficient deep learning for signal and image processing," *IEEE Signal Processing Magazine*, vol. 38, no. 2, pp. 18–44, 2021.
- [13] W. Herzberg, D. B. Rowe, A. Hauptmann, and S. J. Hamilton, "Graph convolutional networks for model-based learning in nonlinear inverse problems," *IEEE Transactions on Computational Imaging*, vol. 7, pp. 1341–1353, 2021.
- [14] J. Xiang, Y. Dong, and Y. Yang, "Fista-net: Learning a fast iterative shrinkage thresholding network for inverse problems in imaging," *IEEE Transactions on Medical Imaging*, vol. 40, no. 5, pp. 1329–1339, 2021.
- [15] F. Colibazzi, D. Lazzaro, S. Morigi, and A. Samoré, "Learning nonlinear electrical impedance tomography," *Journal of Scientific Computing*, vol. 90, no. 1, p. 58, 2022.
- [16] B. Lu, L. Fu, Y. Pan, and Y. Dong, "Swista-nets: Subband-adaptive wavelet iterative shrinkage thresholding networks for image reconstruction," *Computerized Medical Imaging and Graphics*, vol. 113, p. 102345, 2024.
- [17] G. Ma, H. Chen, S. Dong, X. Wang, and S. Zhang, "Pdcista-net: Model-driven deep learning reconstruction network for electrical impedance tomography-based tactile sensing," *IEEE Transactions on Industrial Informatics*, vol. 21, no. 1, pp. 633–642, 2025.
- [18] Q. Zhou, J. Qian, J. Tang, and J. Li, "Deep unrolling networks with recurrent momentum acceleration for nonlinear inverse problems," *Inverse Problems*, vol. 40, no. 5, p. 055014, 2024.
- [19] G. Xu, H. Wang, and Q. Zhou, "Enhancing electrical impedance tomography reconstruction using learned half-quadratic splitting networks with anderson acceleration," *Journal of Scientific Computing*, vol. 98, no. 2, p. 49, 2024.
- [20] Z. Chen, J. Xiang, P.-O. Bagnaninchi, and Y. Yang, "Mmv-net: A multiple measurement vector network for multifrequency electrical impedance tomography," *IEEE Transactions on Neural Networks and Learning Systems*, vol. 34, no. 11, pp. 8938–8949, 2023.
- [21] Z. Wang, T. Zhang, and Q. Wang, "Unrolling reweighted total variation-based split bregman iterative framework for electrical impedance tomography image reconstruction," *IEEE Transactions on Computational Imaging*, vol. 11, pp. 748–763, 2025.
- [22] S. Roychowdhury, M. Diligenti, and M. Gori, "Regularizing deep networks with prior knowledge: A constraint-based approach," *Knowledge-Based Systems*, vol. 222, p. 106989, 2021.
- [23] D. Liu, J. Wang, Q. Shan, D. Smyl, J. Deng, and J. Du, "Deepeit: Deep image prior enabled electrical impedance tomography," *IEEE Transactions on Pattern Analysis and Machine Intelligence*, vol. 45, no. 8, pp. 9627–9638, 2023.
- [24] J. Wang, Y. Wang, J. Deng, and D. Liu, "Unsupervised coordinate-based neural network for electrical impedance tomography," *IEEE Transactions on Computational Imaging*, vol. 9, pp. 1213–1225, 2023.
- [25] Z. Liu, J. Wang, Q. Shan, and D. Liu, "Grapheit: Unsupervised graph neural networks for electrical impedance tomography," *IEEE Transactions on Computational Imaging*, vol. 10, pp. 1559–1570, 2024.
- [26] H. Xia, Q. Shan, J. Wang, and D. Liu, "Nas powered deep image prior for electrical impedance tomography," *IEEE Transactions on Computational Imaging*, vol. 10, pp. 1165–1174, 2024.
- [27] Z. Liu, Z. Chen, H. Fang, Q. Wang, S. Zhang, and Y. Yang, "Regularized shallow image prior for electrical impedance tomography," *IEEE Transactions on Instrumentation and Measurement*, vol. 74, pp. 1–11, 2025.
- [28] J. Wang, J. Deng, and D. Liu, "Deep prior embedding method for electrical impedance tomography," *Neural Networks*, vol. 188, p. 107419, 2025.
- [29] J. Liu, F. Shi, H. Xiong, and Y. Zhou, "Diffusioniteit: Diffusion model for electrical impedance tomography," *IEEE Transactions on Instrumentation and Measurement*, vol. 73, pp. 1–9, 2024.
- [30] S. Shi, R. Kang, and P. Liatsis, "A conditional diffusion model for electrical impedance tomography image reconstruction," *IEEE Transactions on Instrumentation and Measurement*, vol. 74, pp. 1–16, 2025.
- [31] D. Shi, W. Zheng, D. Guo, and H. Liu, "Conditional diffusion model for electrical impedance tomography," *IEEE Transactions on Instrumentation and Measurement*, vol. 74, pp. 1–13, 2025.
- [32] H. Wang, G. Xu, and Q. Zhou, "A comparative study of variational autoencoders, normalizing flows, and score-based diffusion models for electrical impedance tomography," *Journal of Inverse and Ill-posed Problems*, vol. 32, no. 4, pp. 795–813, 2024.
- [33] C. He, Y. Shen, C. Fang, F. Xiao, L. Tang, Y. Zhang, W. Zuo, Z. Guo, and X. Li, "Diffusion models in low-level vision: A survey," *IEEE Transactions on Pattern Analysis and Machine Intelligence*, vol. 47, no. 6, pp. 4630–4651, 2025.
- [34] X. Li, Y. Ren, X. Jin, C. Lan, X. Wang, W. Zeng, X. Wang, and Z. Chen, "Diffusion models for image restoration and enhancement: a comprehensive survey," *International Journal of Computer Vision*, pp. 1–31, 2025.
- [35] X. Zeng, J. Peng, Z. Fu, L. Fan, X. Tu, Y. Huang, and X. Ding, "Accelerating adaptive diffusion and uncertainty modeling for underwater image enhancement," *IEEE Transactions on Multimedia*, pp. 1–15, 2025.
- [36] W. Yu, Q. Liu, Q. Meng, C. Wang, and X. Sun, "D3bsr: Blind super-resolution via diffusion-based disentangled degradation representation," *IEEE Transactions on Multimedia*, pp. 1–15, 2025.
- [37] Y. Qing, S. Liu, H. Wang, and Y. Wang, "Diffuiue: Learning latent global priors in diffusion models for underwater image enhancement," *IEEE Transactions on Multimedia*, vol. 27, pp. 2516–2529, 2025.
- [38] C. Hu, X.-Z. Wei, and X.-J. Wu, "Icdsr: Integrated conditional diffusion model for single image super-resolution," *IEEE Transactions on Multimedia*, pp. 1–13, 2025.
- [39] Y. Wang, J. Sun, H. Liu, X.-P. Zhang, and M. Wei, "Real-scene image dehazing via laplacian pyramid-based conditional diffusion model," *IEEE Transactions on Multimedia*, pp. 1–14, 2025.
- [40] Y. Huang, J. Huang, J. Liu, M. Yan, Y. Dong, J. Lv, C. Chen, and S. Chen, "Wavedm: Wavelet-based diffusion models for image restoration," *IEEE Transactions on Multimedia*, vol. 26, pp. 7058–7073, 2024.
- [41] L. Zhao, J. Wang, C. Fan, Z. Zheng, and X. Zhang, "Frequency-conditional diffusion model for low-light image enhancement," *Neurocomputing*, p. 131383, 2025.

- [42] F. Luo, X. Chen, C. Fu, T. Guo, and B. Du, "Hdiff-hir: Hierarchically conditional diffusion model for hyperspectral image reconstruction," *IEEE Transactions on Circuits and Systems for Video Technology*, pp. 1–1, 2025.
- [43] D. Xie, X. Hu, H. Xiao, Y. Zhou, and S. Duan, "Reffusion: enhancement conditional diffusion framework with dual domain interaction transformer for image restoration," *Knowledge-Based Systems*, vol. 311, p. 112998, 2025.
- [44] L. Liu, J. Zou, C. Xu, K. Wang, J. Lyu, X. Xu, Z. Hu, and J. Qin, "Im-diff: Implicit multi-contrast diffusion model for arbitrary scale mri super-resolution," *IEEE Journal of Biomedical and Health Informatics*, vol. 29, no. 6, pp. 4200–4212, 2025.
- [45] Y. Zhang, L. Li, J. Wang, X. Yang, H. Zhou, J. He, Y. Xie, Y. Jiang, W. Sun, X. Zhang *et al.*, "Texture-preserving diffusion model for cbct-to-ct synthesis," *Medical Image Analysis*, vol. 99, p. 103362, 2025.
- [46] G. Webber and A. J. Reader, "Diffusion models for medical image reconstruction," *BJR—Artificial Intelligence*, vol. 1, no. 1, p. ubae013, 2024.
- [47] Q. Wang, Y. Cai, H. Yu, F. Liu, and W. Wu, "Misd: Model-informed stable diffusion model for limited noisy data ct reconstruction," *IEEE Transactions on Computational Imaging*, vol. 11, pp. 1434–1446, 2025.
- [48] Q. Gao, Z. Chen, D. Zeng, J. Zhang, J. Ma, and H. Shan, "Noise-inspired diffusion model for generalizable low-dose ct reconstruction," *Medical Image Analysis*, vol. 105, p. 103710, 2025. [Online]. Available: <https://www.sciencedirect.com/science/article/pii/S1361841525002579>
- [49] Z. Zhou, T. Liu, B. Yu, Y. Gong, L. Shi, and Q. Liu, "Physics-informed deepct: Sinogram wavelet decomposition meets masked diffusion," *arXiv preprint arXiv:2501.09935*, 2025.
- [50] B. Guan, C. Yang, L. Zhang, S. Niu, M. Zhang, Y. Wang, W. Wu, and Q. Liu, "Generative modeling in sinogram domain for sparse-view ct reconstruction," *IEEE Transactions on Radiation and Plasma Medical Sciences*, vol. 8, no. 2, pp. 195–207, 2024.
- [51] C. Fang, Y. Liu, B. Morovati, S. Han, Y. Shi, L. Zhou, S. Fan, and H. Yu, "Respf: Residual poisson flow generative model for efficient and physically consistent sparse-view ct reconstruction," *IEEE Transactions on Radiation and Plasma Medical Sciences*, pp. 1–1, 2025.
- [52] H. Chung and J. C. Ye, "Score-based diffusion models for accelerated mri," *Medical image analysis*, vol. 80, p. 102479, 2022.
- [53] Y. Guan, K. Zhang, Q. Qi, D. Wang, Z. Ke, S. Wang, D. Liang, and Q. Liu, "Zero-shot dynamic mri reconstruction with global-to-local diffusion model," *NMR in Biomedicine*, vol. 38, no. 10, p. e70128, 2025.
- [54] G. Oh, S. Jung, J. E. Lee, and J. C. Ye, "Annealed score-based diffusion model for mr motion artifact reduction," *IEEE Transactions on Computational Imaging*, vol. 10, pp. 43–53, 2024.
- [55] C. Cao, Z.-X. Cui, Y. Wang, S. Liu, T. Chen, H. Zheng, D. Liang, and Y. Zhu, "High-frequency space diffusion model for accelerated mri," *IEEE Transactions on Medical Imaging*, vol. 43, no. 5, pp. 1853–1865, 2024.
- [56] J. Wang, Z. Shi, X. Gu, Y. Yang, and J. Sun, "Diffusion-based arbitrary-scale magnetic resonance image super-resolution via progressive k-space reconstruction and denoising," *Medical Image Analysis*, p. 103814, 2025.
- [57] D. Kong, H. Yang, Y. Luo, Z. Chen, B. Lei, Y. Zhong, M. Liu, Y. Chen, and C. Ma, "D-star: Diffusion-based sparse tomographic angular recovery for isotropic-resolution photoacoustic imaging," *IEEE Transactions on Medical Imaging*, vol. 44, no. 11, pp. 4404–4416, 2025.
- [58] J. Lin, Z. Li, H. Fang, G. Liu, S. Cao, Y. Cao, L. Li, J. Li, Y. Wang, H. Wei *et al.*, "Enhanced score-based priors-boosted generative model for resolution breakthrough in photoacoustic tomography," *Optics Letters*, vol. 50, no. 15, pp. 4750–4753, 2025.
- [59] X. Song, X. Zou, K. Zeng, J. Li, S. Hou, Y. Wu, Z. Li, C. Ma, Z. Zheng, K. Guo *et al.*, "Multiple diffusion models-enhanced extremely limited-view reconstruction strategy for photoacoustic tomography boosted by multi-scale priors," *Photoacoustics*, vol. 40, p. 100646, 2024.
- [60] S. Dey, S. Saha, B. T. Feng, M. Cui, L. Delisle, O. Leong, L. V. Wang, and K. L. Bouman, "Score-based diffusion models for photoacoustic tomography image reconstruction," in *ICASSP 2024 - 2024 IEEE International Conference on Acoustics, Speech and Signal Processing (ICASSP)*, 2024, pp. 2470–2474.
- [61] Z. Li, J. Lin, Y. Wang, J. Li, Y. Cao, X. Liu, W. Wan, Q. Liu, and X. Song, "Ultra-sparse reconstruction for photoacoustic tomography: Sinogram domain prior-guided method exploiting enhanced score-based diffusion model," *Photoacoustics*, vol. 41, p. 100670, 2025.
- [62] H. Verinaz-Jadan and S. Yan, "Integrating deep unfolding with direct diffusion bridges for computed tomography reconstruction," *arXiv preprint arXiv:2409.09477*, 2024.
- [63] M. U. Mirza, O. Dalmaç, H. A. Bedel, G. Elmas, Y. Korkmaz, A. Güngör, S. U. Dar, and T. Çukur, "Learning fourier-constrained diffusion bridges for mri reconstruction," *arXiv preprint arXiv:2308.01096*, 2023.
- [64] Y. Wang, P. Jin, S. Yoon, M. Tivnan, Q. Li, L. Zhang, and D. Wu, "Measurement embedded schrodinger bridge for inverse problems," *arXiv preprint arXiv:2407.04162*, 2024.
- [65] Y. Wang, P. Jin, S. Yoon, M. Tivnan, S. Zhang, L. Zhang, Q. Li, Z. Chen, and D. Wu, "Projection embedded diffusion bridge for ct reconstruction from incomplete data," *arXiv preprint arXiv:2510.22605*, 2025.
- [66] B. Sobieski, M. Tivnan, Y. Wang, S. yoon, P. Jin, D. Wu, Q. Li, and P. Biecek, "System-embedded diffusion bridge models," in *The Thirty-ninth Annual Conference on Neural Information Processing Systems*, 2025. [Online]. Available: <https://openreview.net/forum?id=cipx3rwfWp>
- [67] Y. Hu, A. Peng, W. Gan, and U. S. Kamilov, "Adobi: Adaptive diffusion bridge for blind inverse problems with application to mri reconstruction," *arXiv preprint arXiv:2411.16535*, 2024.